Journal of Materials Chemistry A

PAPER

View Article Online
View Journal

Cite this: DOI: 10.1039/c4ta02558j

Peroxide defect formation in zirconate perovskites

S. C. Middleburgh,*[a] I. Karatchevtseva,[a] B. J. Kennedy,[b] P. A. Burr,[c] Z. Zhang,[a] E. Reynolds,[b] R. W. Grimes[c] and G. R. Lumpkin[a]

Received 22nd May 2014
Accepted 2nd August 2014

DOI: 10.1039/c4ta02558j

www.rsc.org/MaterialsA

Atomic scale modelling suggests that excess oxygen can be accommodated in the group II perovskite zirconates by the formation of peroxide ion defects. This is unprecedented given the lack of charge compensating defects required for standard excess oxygen accommodation. The solution energy of O_2 was predicted to be close to zero for $BaZrO_3$, accommodating the peroxide ion defect more easily than in $SrZrO_3$ or $CaZrO_3$. This was experimentally examined by exposing $SrZrO_3$ and $BaZrO_3$ to hydrogen peroxide solution and then carrying out Raman spectroscopy measurements to look for a peak indicative of peroxide ions. A peak was observed at ~1000 cm^{-1} in both compositions, suggesting the theoretically predicted peroxide ion is present.

1 Introduction

Excess oxygen has often been dismissed as a likely mechanism for non-stoichiometry in group II perovskite zirconates due to the lack of a positive charge balancing defect. It is not surprising, therefore, that the focus of a great deal of previous work has aimed to understand the movement of vacancies and other defects through these technologically important materials. Compounds that have the perovskite structure, with general formula ABO_3, are of great interest in a number of key sectors including photovoltaics, solid-oxide fuel cells and the nuclear industry.[1,2] Zirconate perovskites are of particular interest due to their stability at high temperatures (>1300 °C),[3] chemical inertness and proton conductivity.[4] $BaZrO_3$ and $SrZrO_3$, when doped, exhibit high proton conductivities and thus have potential uses as electrolytes in mid-temperature fuel cells.[5] The high proton conductivities are promoted by the reduction in oxygen stoichiometry as a result of doping trivalent cations onto tetravalent cation sites forming $ABO_{3-\delta}$.[6] The perovskite zirconates also have importance in the nuclear fuel cycle: Ba, Sr and Zr are produced as a result of the fission of U^{235} in UO_2, the most common fuel type. This production of Ba, Sr and Zr results in the formation of secondary phases in UO_2 fuels, commonly referred to as 'grey phases'.[7] These grey phases contain $BaZrO_3$ as well as the mixed cation zirconate, (Sr, Ba)ZrO_3.

Peroxide defects have been identified in a number of binary oxides but not in ternary compounds such as perovskites. The versatility of the peroxide ion is highlighted by its preferred formation over other defects in MgO and other group II binary oxides .[8] This is mainly due to the fact that the excess oxygen is part of a molecule, O_2^{2-}, which has the same charge as the lattice O^{2-} ion. Often when oxygen is accommodated as a single interstitial species, O^{2-}, cations assume higher charge, but this is not possible for all cations. For example, CeO_2 and ThO_2 cannot accommodate O^{2-} interstitial defects, since neither Ce^{4+} nor Th^{4+} can be easily oxidised to their +5 valence states.[9]

Recent work by Ren, Masó and West[10] has indicated that excess oxygen can be accommodated in the defect perovskite, $BaTi_{1-x}Ca_xO_{3-x+\delta}$, when heated under high pressure and highly oxidising environments. It is supposed that this accommodation proceeds by filling the oxygen vacancies, formed as a result of the aliovalent Ca^{2+} doping, with superoxide, O_2^- ions. This behaviour was investigated using Raman spectroscopy; the superoxide was identified by the formation of a peak around 1125 cm^{-1}.[10]

X-ray and neutron diffraction results indicated that at room temperature the long-range crystal structure of $BaZrO_3$ is cubic in space group $Pm\bar{3}m$,[11] while $SrZrO_3$ and $CaZrO_3$ have the orthorhombic structure in *Pbnm*.[11–13] However, recent computational studies have shown that the observed cubic structure for $BaZrO_3$ is unfavourable compared to a lower symmetry arrangement, which spontaneously relaxed from the cubic arrangement.[14–16] It has also been shown that the observed Raman spectrum from $BaZrO_3$ agrees with tetragonal and orthorhombic type of local structure.[17,18] The cubic phase of $BaZrO_3$ is not expected to have any first order Raman active modes, similar to the cubic structured $SrTiO_3$.[19] The tetragonal *I4/mcm* structure (observed to be the high pressure phase of $BaZrO_3$ (ref. 20)) has been calculated to be more favourable than the cubic $Pm\bar{3}m$ structure in recent DFT calculations (supported by EXAFS studies).[14]

In the present work we intend to highlight the flexibility of the peroxide defect by showing that it can be accommodated in

[a]Australian Nuclear Science and Technology Organisation, Locked Bag 2001, Kirrawee DC, NSW 2232, Australia. E-mail: simon.middleburgh@hotmail.co.uk; Tel: +61 424862208

[b]Department of Chemistry, University of Sydney, Sydney, NSW 2006, Australia

[c]Department of Materials, Imperial College London, South Kensington, London, SW7 2AZ, UK

ternary oxides as well as the binary oxides that were previously considered. We will consider the series of simple perovskite zirconates: $BaZrO_3$, $SrZrO_3$ and $CaZrO_3$. For these compounds, we discuss the arrangement of the peroxide defects and the effect it may have on the anion migration. Theoretical techniques are used to predict the energies and structures associated with the peroxide species in the perovskite structure, while experiments (here Raman measurements) are used in synergy with the modelling effort in the 'grey phase' zirconates, $BaZrO_3$ and $SrZrO_3$.

2 Methodology

2.1 Computational methods

Calculations to understand the drive for the peroxide defect formation in group II zirconate perovskites were carried out using the density functional theory (DFT) code, VASP.[21] A 4 × 4 × 4 Γ-centred k-point grid was used for all calculations. The calculations employed the generalised gradient approximation exchange-correlation functional with projector augmented wave (GGA-PAW) pseudopotentials provided with the VASP package,[22] taking care to use those with the greatest number of valence electrons.

We have considered both low symmetry tetragonal and orthorhombic structures for $BaZrO_3$, but only the orthorhombic structure for $SrZrO_3$ and $CaZrO_3$. While the tetragonal structure was modelled using a 3 × 3 × 3 supercell of the cubic structure containing 135 lattice sites (which relaxed to a single tetragonal supercell), the orthorhombic structure was produced using a 2 × 2 × 1 supercell of the *Pbnm* structure containing 80 lattice sites. Simulations indicate that the low symmetry tetragonal and orthorhombic arrangements are considerably more favourable for $BaZrO_3$ when compared to its ideal cubic structure (both within 10^{-3} eV per formula unit of each other and >0.2 eV more favourable than a forced, ideal cubic arrangement).

Defect formation energies E_f for defects D with charge q were calculated following eqn 1.

$$E_f = E_{D,q} - E_P + \frac{1}{2}\mu_{O_2} + q\mu_e + E_{MP} \quad (1)$$

where E_P and $E_{D,q}$ are the total energies from the perfect and defective DFT simulations, μ_{O_2} is the chemical potential of an O_2 molecule, μ_e is the Fermi level aligned to the valence band maximum, and E_{MP} is the Makov–Payne correction term for charge interaction in the periodic boundary charge interaction.[23] For charge neutral defects, the latter two terms are zero. μ_{O_2} was calculated from the experimental binding energy of O_2, 2.56 eV.[24] The dielectric constant for the Makov–Payne correction was also taken from experiment.[25]

Climbing image nudged elastic band calculations[26] were carried out to determine the energy barrier for the migration of additional oxygen in the low symmetry tetragonal $BaZrO_3$ structure and all orthorhombic structures. Transport in the ⟨100⟩ and ⟨110⟩ pseudo-cubic directions was considered, each with five intermediate points along the reaction coordinate (allowing one to be near the expected maximum).

The vibrational wavenumber associated with the peroxide defect in the perovskites studied was predicted. The relaxed peroxide ion was stretched and compressed on its axis by four increments of 0.5%. The resulting energy was plotted against distance and a harmonic function fitted to the data to yield the harmonic force constant of the peroxide ion (k). The wavenumber (ν) can be calculated from the force constant:

$$\nu = \left(\frac{k(2m)}{4\pi^2 c^2 m^2}\right)^{\frac{1}{2}} \quad (2)$$

where c is the speed of light in a vacuum and m is the mass of oxygen atom. This value can be compared to experimental spectroscopic data to identify the presence of peroxide defects.

2.2 Experimental methods

2.2.1 Powder production. Stoichiometric quantities of high-purity $SrCO_3$ or $BaCO_3$ were mixed with ZrO_2 in an acetone slurry and ground, using a mortar and pestle, until dry. The homogeneous Sr containing mixture was then compressed in alumina crucibles and heated in air at 800 °C for 24 hours, at 1200 °C for 24 hours, and finally at 1400 °C for 96 hours with periodic regrinding, mixing, and pressing.[13] The Ba containing mixture was calcined at 1000 °C for 24 hours, pressed into a pellet and then heated at 1400 °C for 24 hours. The products were shown to be phase pure using powder X-ray diffraction measurements – the $BaZrO_3$ having the cubic $Pm\bar{3}m$ structure and the $SrZrO_3$ taking the orthorhombic *Pbnm* structure.

2.2.2 H_2O_2 powder treatment. Finely ground powders of the two zirconate perovskites ($BaZrO_3$ and $SrZrO_3$) were treated in 30 wt% H_2O_2 solution for 150 hours. The resulting slurries were kept refrigerated at 277 K to retard the natural decomposition of H_2O_2 into H_2O and $\frac{1}{2}O_2$. Before Raman analysis, the powders were thoroughly dried on filter paper.

2.2.3 Raman spectroscopy. Raman spectra were collected using a spectrometer equipped with a mono-chromator, a filter system and a Peltier-cooled Charge-Coupled Device (CCD). Powders were excited by an argon ion laser (514.5 nm) and collected in the range of 2000–100 cm^{-1} with a spectral resolution of ~1.7 cm^{-1} for the 1800 l mm^{-1} grating as theoretical calculations suggest that all Raman active modes for these ionic perovskites and the peroxide O_2^{2-} defect vibration are within the above wavenumber range. The spot size was around 1.5 μm for 50× magnification. Spectra were calibrated using the 520.5 cm^{-1} line of a silicon wafer.

To mitigate against confusing H_2O_2 or H_2O retained on the surface of the powder with any other peaks that may form (particularly the peroxide ion peak), the Raman spectrum for the H_2O_2 solution was also measured. It produces a strong single peak at 877 cm^{-1} and two others at 3425 and 3254 cm^{-1} (the latter two are outside the measurement range for the powders). Any Raman active modes that appear after H_2O_2 treatment that are distinct from the H_2O_2 modes are investigated as modes of specific interest.

3 Results

3.1 Density functional theory predictions

3.1.1 Tetragonal $BaZrO_3$. Excess oxygen can enter a system by the formation of interstitial species or peroxide species. In a similar manner to previous work, the solution energy of oxygen from an O_2 molecule is a good measure of the drive for excess oxygen accommodation in the ABO_3 compound.[9] Oxygen solution in the form of interstitial defects (eqn 3), split interstitials (eqn 4) or peroxide defects (eqn 5) is possible. The key difference between the split interstitial and the peroxide ion formation is the bond distance, the peroxide bond distance is expected to be 1.49 Å (the distance calculated in other ionic solids[8]) whereas the split interstitial O–O distance is expected to be larger (~2 Å).

$$\frac{1}{2}O_2 \rightarrow O_i \quad (3)$$

$$\frac{1}{2}O_2 + O_O \rightarrow \{V_O : 2O_i\}_{\text{split interstitial}} \quad (4)$$

$$\frac{1}{2}O_2 + O_O \rightarrow \{V_O : 2O_i\}_{\text{peroxide ion}} \quad (5)$$

Oxygen solution *via* reaction 5 was calculated to be the most favourable, proceeding with an energy of −0.01 eV (within the error of the calculation method, we interpret this to be approximately zero) while the oxygen interstitial and split interstitial were predicted to both spontaneously relax (*via* the energy minimisation calculation) to the neutral peroxide defect from the initial defect positions. Finding that the peroxide defect is favourable is not surprising given the absence of a simple charge balancing defect in $BaZrO_3$ (in contrast to, for example, U^{5+} ion formation in UO_2 (ref. 27)).

Charged defects were briefly considered in the low symmetry tetragonal $BaZrO_3$ to understand the change in preferred defect formation as a function of Fermi level energy. At the top of the valence band (0 eV in Fig. 1) the formation energy for the most favourable peroxide defect is −0.01 eV. As the Fermi energy is increased towards the bottom of the conduction band (~3.10 eV as calculated by our computational methods), the charged single defects O_i' and O_i'' become favourable. This suggests that in the presence of a charged defect, such as an extrinsic defect or oxygen vacancy, the charged O_i'' will be preferred. When considering the experimentally observed larger band gap of ~5 eV in $BaZrO_3$,[28] the charged O_i'' is still preferred over the other defects considered.

Two simple migration processes between adjacent sites in the tetragonal structure were identified for the peroxide ion: the ⟨100⟩ and ⟨110⟩ pseudo-cubic directions. In both cases the peroxide ion is split and reformed. Both mechanisms are illustrated in Fig. 2. Migration was predicted to proceed with an energy barrier of 2.03 eV and 0.78 eV in the ⟨100⟩ and ⟨110⟩ directions, respectively. The energy profiles are illustrated in Fig. 3 where a spike is indicated in both processes as a result of the breaking of the O_2^{2-} ion into two non-covalently bound defects. The migration is far more favourable in the ⟨110⟩ direction and has a similar value to those computed for oxygen vacancy migration in other perovskites including 0.8 eV in $LaMnO_3$,[29] between 0.73–1.22 eV in a number of $LaXO_3$ compounds (where X is Co, Ga, Y or Mn),[30] 0.9 eV in $SrTiO_3$ (ref. 31) and 0.71 eV in cubic $BaZrO_3$.[32] As the peroxide defect is not charged, the migration of the peroxide species is not considered as a charge carrier (as it is for oxygen vacancies). Nevertheless, they may play a significant role in the behaviour of a number of charged defects, as vacancy formation could be retarded as a consequence of peroxide ions being present in the system.

3.1.2 Orthorhombic $BaZrO_3$, $SrZrO_3$ and $CaZrO_3$. Equivalently to eqn 3–5, excess oxygen was modelled by introducing interstitials, split interstitials and peroxide ions into the orthorhombic $BaZrO_3$, $SrZrO_3$ and $CaZrO_3$ lattices. The split interstitials and peroxide ions were centred over the two symmetrically distinct oxygen sites in the *Pbnm* structure and orientated along the three equivalent ⟨110⟩ directions (when considered in a pseudo-cubic orientation).

Similarly to tetragonal $BaZrO_3$, peroxide defects are predicted to be most favourable. There was essentially zero

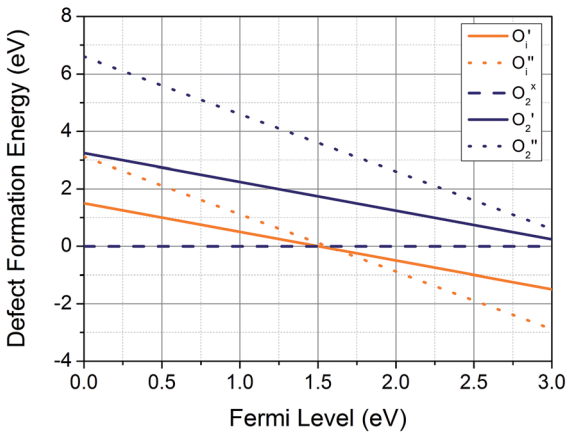

Fig. 1 Excess oxygen defect formation energy in $BaZrO_3$ as a function of Fermi energy from the top of the valence band to the bottom of the conduction band. Two types of defects are considered, oxygen interstitials (red) and two-oxygen complexes (blue) (where the $O_2^{\times}$ is the peroxide ion).

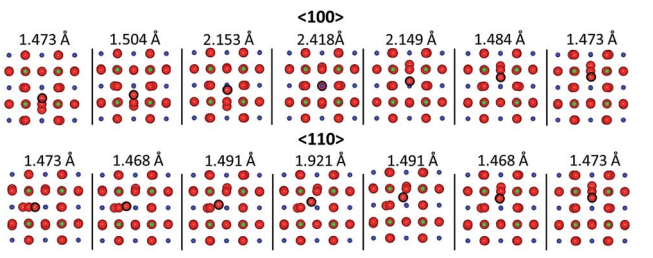

Fig. 2 Migration of a constituent oxygen in a peroxide ion in tetragonal $BaZrO_3$ from one site to another in the ⟨100⟩ and ⟨110⟩ pseudo-cubic directions. The shortest O–O bond distance of the migrating oxygen is shown for each snapshot, the length of ~1.47 Å corresponds to the expected peroxide bond length. Oxygen species are represented by large red spheres, zirconium as small blue spheres and barium as small green spheres.

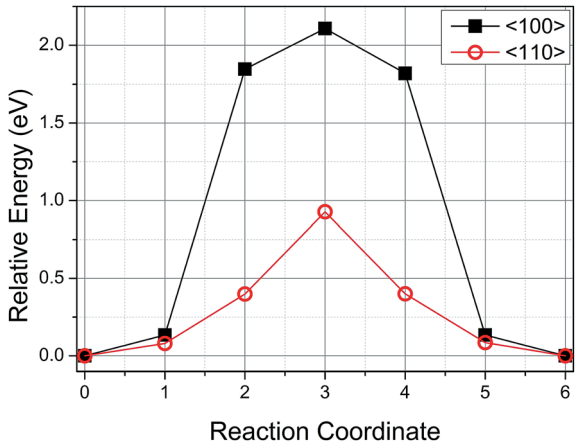

Fig. 3 Variation in system energy of tetragonal $BaZrO_3$ as a constituent oxygen from a peroxide ion migrates in the ⟨100⟩ (black square) and ⟨110⟩ (red circle) directions (in the pseudo-cubic setting). The migration pathway is sampled at five steps along the reaction coordinate.

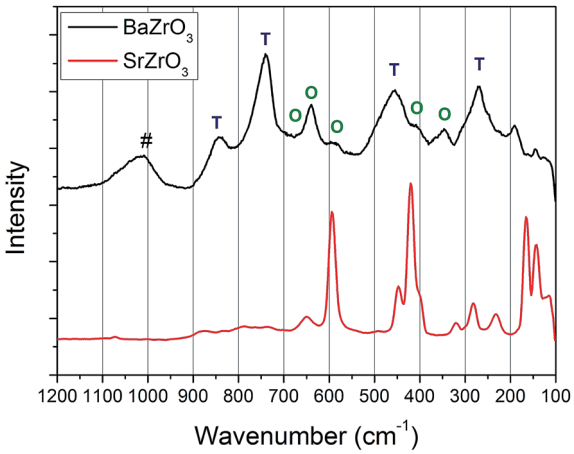

Fig. 4 Raman specra of $BaZrO_3$ (black) and $SrZrO_3$ (red) from powder samples before treatment with H_2O_2. The tetragonal (T) and orthorhombic (O) peaks are shown for the $BaZrO_3$ powder (assigned according to[17]). The peak labelled by # is assigned to the O_2^{2-} stretching mode within the $BaZrO_3$ crystal.

dependency on orientation or site (*i.e.* a variation of less than 0.01 eV was observed, which is within the uncertainty of the method). All split interstitial and isolated interstitial defect arrangements were observed to re-arrange and produce a peroxide ion. The reaction for the incorporation of $\frac{1}{2}O_2$ into $BaZrO_3$, $SrZrO_3$ and $CaZrO_3$ (equivalent to eqn 5) proceeds with energies of 0.06 eV, 0.10 eV and 0.22 eV, respectively.

Since the solution energy of $\frac{1}{2}O_2$ is small and positive for $CaZrO_3$ and $SrZrO_3$ whilst negligible for $BaZrO_3$, it is reasonable to expect that it should be possible to prepare oxides of the type $AZrO_{3+\delta}$, although the vibrational entropy of the gas phase O_2 molecule will drive against this to some extent.[8] The reaction of H_2O_2 with a lattice O^{2-} ion will release H_2O and O_2^{2-} peroxide ion, yielding approximately 1 eV (ref. 8) further favouring the reaction.

Migration was considered in all three compounds along an equivalent path to the preferred ⟨110⟩ migration predicted in tetragonal $BaZrO_3$. Migration activation enthalpies in all of the orthorhombic structures were similar to that in tetragonal $BaZrO_3$. Orthorhombic $BaZrO_3$ exhibits the smallest barrier, 0.75 eV, followed by $SrZrO_3$ and $CaZrO_3$ with similar energies of 0.82 eV and 0.83 eV, respectively. These are moderate energy barriers and suggest that transport will be rapid at high temperatures but sluggish at room temperature.

3.2 Raman spectroscopy of H_2O_2 treated samples

Raman spectra of $SrZrO_3$ and $BaZrO_3$ were measured for the as-prepared powders and for powders treated with H_2O_2. The Raman spectra for the untreated powders are provided in Fig. 4, in good agreement with previously reported spectra.[17,18,33,34] In the orthorhombic *Pbnm* structure 24 Raman active modes are expected, although not all of these will result in observable bands, due either to overlap with more intense measures, or if they have very low polarisability as that precludes observable intensity. We observe 10 well resolved bands in agreement with the recent studies of Slodczyk *et al.*[34] The band at 600 cm^{-1} is believed to be due to the Zr–O stretch mode, and the bands around 420 cm^{-1} are related to Zr–O torsional modes. The bands between 100–200 cm^{-1} are associated with oxygen octahedral rotations.

The Raman spectrum of $BaZrO_3$ is distinctly different from that of $SrZrO_3$. An ideal cubic ABO_3 perovskite structure should not show any first order Raman peaks, although broad second-order scattering features have been observed in cubic perovskites such as $SrTiO_3$.[19] It is possible that the complex Raman spectrum observed for $BaZrO_3$ is indicative of the presence of micro-domains of lower symmetry or local distortions of the cubic lattice, as postulated in past work.[17,18] Our calculations, described above, suggest that symmetry lowering is likely in $BaZrO_3$. Following Kim *et al.*[17] we have tentatively labelled the peaks in the Raman spectra as coming from tetragonal (T) or orthorhombic (O) micro-domains. The presence of such micro-domains is at variance with the recent study of Rabuffetti and Brutchey[35] who, using both X-ray absorption near edge structure and pair distribution function analysis of X-ray total scattering data, concluded that nanoparticles of $BaZrO_3$ are cubic and this is clearly worthy of further study.

More critical is the presence of a broad peak near 1000 cm^{-1} in the Raman spectra of $BaZrO_3$, that is absent in the Raman spectra of $SrZrO_3$. This feature has been observed in previous studies of $BaZrO_3$ (the origin of which was not identified)[17] and the frequency is inconsistent with any first order scattering features, irrespective of the symmetry.

The negligible energy required to incorporate additional O_2 into $BaZrO_3$ would be consistent with the feature observed in the Raman spectra near 1000 cm^{-1} being due to a peroxide defect. Atomic scale modelling was used to estimate the bond strength of a peroxide ion in tetragonal $BaZrO_3$ and hence the wavenumber of the Raman active stretch mode associated with

the peroxide defect. The method predicts the O–O stretching mode in $BaZrO_3$ to have a frequency of 996 cm^{-1} in the tetragonal structure or 985 cm^{-1} in the orthorhombic structure. These values are in good agreement with the observed feature in the Raman spectra of $BaZrO_3$, although care must be taken when estimating bond strengths by DFT using GGA exchange correlation as the bond strengths are often under-predicted.[36]

Care must also be taken when analysing the Raman data as the broad peak may be a result of a number of other defect species. The peak may be consistent with not only the predicted peroxide species in the bulk but also carbonate (~1065–1100 cm^{-1} (ref. 37)) and nitrate species (1044 cm^{-1} (ref. 38)). In fact, previous work found that excess oxide species on oxide surfaces will functionalise the surface and promote the formation of carbonate species in the presence of CO_2.[37]

The presence of excess oxygen in the $BaZrO_3$ is expected even without reaction with H_2O_2, given the negligible energy for oxygen solution from O_2 gas *via* peroxide defects (Section 3.1). In an attempt to increase the amount of excess oxygen in the system further, a powder sample of $BaZrO_3$ was treated with H_2O_2 for one week and the Raman spectrum re-examined. The Raman spectrum of this treated sample did not contain any additional features however the peak near 1000 cm^{-1} was observed to increase in intensity (~5%) although this increase can probably be treated within the error of the experimental method.

Raman spectra for $SrZrO_3$ measured for up to 12 hours after treatment with H_2O_2 are illustrated in Fig. 5. A large peak at 877 cm^{-1} (labelled with a *) was observed in the freshly treated sample and this is observed to decrease in intensity over time.

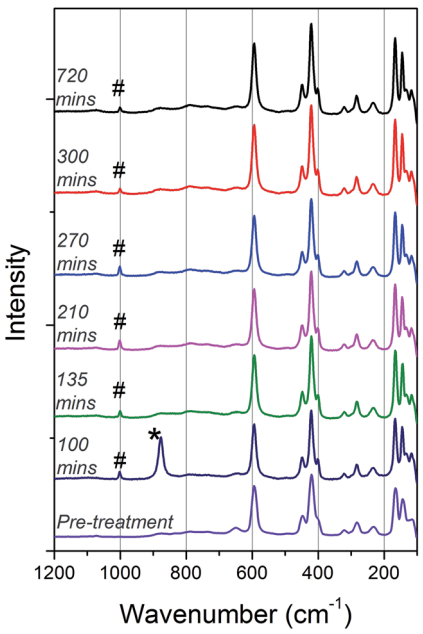

Fig. 5 Raman specra of $SrZrO_3$ treated with H_2O_2 taken at various times after removal from H_2O_2 solution. The peak labelled with * is assigned to the H_2O_2 solution. The peak labelled with # is assigned to the peroxide ion in the $SrZrO_3$ lattice.

This feature is attributed to H_2O_2 and the reduction in intensity is probably as a result of the decomposition of the molecule in air. The remaining peaks in the Raman spectra of treated $SrZrO_3$ sample are very similar to those seen in the spectrum of the untreated powder with the exception of a peak near 1000 cm^{-1}. This peak is attributed to the presence of peroxide ions, as simulations estimate the peak associated with the stretching mode of a peroxide ion in $SrZrO_3$ to be at 980 cm^{-1}.

4 Summary

This work predicts that the dominant defect by which excess oxygen is accommodated in $BaZrO_3$, $SrZrO_3$ and $CaZrO_3$ is the peroxide ion. Atomic scale modelling predicts that the solution of O_2 gas proceeds favourably into $BaZrO_3$, but is less favourable in $SrZrO_3$ which in turn is more favourable than $CaZrO_3$. Despite the change in predicted solubility through the group, the maximum solution enthalpy for $\frac{1}{2}O_2$ in $CaZrO_3$ is still only 0.22 eV. The transport of the excess oxygen through the perovskite lattice was predicted to proceed with activation energies of less than 1 eV in each of the systems. We also predict that the defect accommodating excess oxygen in $BaZrO_3$ will change as a function of Fermi energy, peroxide defects being preferred at the top of the valence band and charged oxygen interstitials being preferred at the bottom of the conduction band.†

Experimentally, $SrZrO_3$ and $BaZrO_3$ were investigated by Raman spectroscopy before and after treatment with hydrogen peroxide solution. This increased the oxygen partial pressure and in doing so allowed oxygen uptake into the systems to proceed more favourably. A peak, with a value consistent with the modelling predictions for an O_2^{2-} ion inside the $SrZrO_3$ lattice was identified after treatment.

Interestingly, a peak associated with the O_2^{2-} ion in $BaZrO_3$ was present in the Raman spectrum even before treatment with H_2O_2. This result was not unexpected given the negligible solution enthalpy of $\frac{1}{2}O_2$ into $BaZrO_3$. The Raman spectrum of $BaZrO_3$ had features inconsistent with the cubic symmetry of the system as determined by X-ray diffraction – this remains unexplained but may be due to either local distortions in the lattice at room temperature or a result of the peroxide ion population in the material forcing a deviation from the ideal cubic structure.

Future work will be focused on quantifying the amount of excess oxygen that is accommodated in the zirconates, including $CaZrO_3$, as well as understanding the effect of the peroxide defect on the observed crystal structure.

By combining the theoretical approach with experimental Raman data, we conclude that peroxide ion defects can form (and are the most favourable defect) in both $BaZrO_3$ and $SrZrO_3$, and the stoichiometry of the materials is $AZrO_{3+\delta}$.

† Whilst this work was under peer review, a manuscript by Chen and Umezawa has been published that predicts the ease of formation of O_2^{2-} defects in $SrTiO_3$ using DFT calculations with similar conclusions to our work.[39] They investigate the defect as an alternative to compensate acceptor doping in $SrTiO_3$.

Acknowledgements

Dr Lou Vance is thanked for his advice and help with manufacturing the powders used in this study. Dr Gordon Thorogood is also thanked for his discussions on the crystallography related to the perovskite systems. This work was supported by the Multi-modal Australian ScienceS Imaging and Visualisation Environment (MASSIVE) (https://www.massive.org.au).

References

1 R. H. Mitchell, *Perovskites: modern and ancient*, Almaz Press Inc., 2002.
2 M. L. Fullarton, M. J. Qin, M. Robinson, N. A. Marks, D. J. M. King, E. Y. Kuo, G. R. Lumpkin and S. C. Middleburgh, *J. Mater. Chem. A*, 2013, **1**, 14633–14640.
3 R. Vassen, X. Cao, F. Tietz, D. Basu and D. Stöver, *J. Am. Ceram. Soc.*, 2000, **83**, 2023–2028.
4 E. Fabbri, L. Bi, H. Tanaka, D. Pergolesi and E. Traversa, *Adv. Funct. Mater.*, 2011, **21**, 158–166.
5 K. D. Kreuer, St. Adams, W. Münch, A. Fuchs, U. Klock and J. Maier, *Solid State Ionics*, 2001, **145**, 295–306.
6 J. Wu, R. A. Davies, M. S. Islam and S. M. Haile, *Chem. Mater.*, 2005, **17**, 846–851.
7 H. Kleykamp, *J. Nucl. Mater.*, 1985, **131**, 221–246.
8 S. C. Middleburgh, K. P. D. Lagerlof and R. W. Grimes, *J. Am. Ceram. Soc.*, 2013, **96**, 308–311.
9 S. C. Middleburgh, G. R. Lumpkin and R. W. Grimes, *Solid State Ionics*, 2013, **253**, 119–122.
10 P. Ren, N. Masó and A. R. West, *Phys. Chem. Chem. Phys.*, 2013, **15**, 20943.
11 I. Levin, T. G. Amos, S. M. Bell, L. Farber, T. A. Vanderah, R. S. Roth and B. H. Toby, *J. Solid State Chem.*, 2003, **175**, 170.
12 C. J. Howard, K. S. Knight, B. J. Kennedy and E. H. Kisi, *J. Phys.: Condens. Matter*, 2000, **12**, L677.
13 T. K. Y. Wong, B. J. Kennedy, C. J. Howard, B. A. Hunter and T. Vogt, *J. Solid State Chem.*, 2001, **156**, 255–263.
14 A. I. Lebedev and I. A. Sluchinskaya, *Phys. Solid State*, 2013, **55**, 1941.
15 J. W. Bennett, I. Grinberg and A. M. Rappe, *Phys. Rev. B: Condens. Matter Mater. Phys.*, 2006, **73**, 180102.
16 A. Bilić and J. D. Gale, *Phys. Rev. B: Condens. Matter Mater. Phys.*, 2009, **79**, 174107.
17 D. Y. Kim, E. D. C. Patrik, S. Miyoshi, T. Tsuchita and S. Yamaguchi, *Pacific Rim Meeting (PRiME) on Electrochemical and Solid-State Science*, The Electrochemical Society, 2012, Abstract 2098.
18 F. Giannici, M. Shirpour, A. Longo, A. Martorana, R. Merkle and J. Maier, *Chem. Mater.*, 2011, **23**, 2994.
19 W. G. Nilsen and J. G. Skinner, *J. Chem. Phys.*, 1968, **48**, 2240.
20 X. Yang, Q. Li, R. Liu, B. Liu, H. Zhang, S. Jiang, J. Liu, B. Zou, T. Cui and B. Liu, *J. Appl. Phys.*, 2014, **115**, 124907.
21 G. Kresse and J. Hafner, *Phys. Rev. B: Condens. Matter Mater. Phys.*, 1993, **47**, 558.
22 J. P. Perdew, K. Burke and M. Ernzerhof, *Phys. Rev. Lett.*, 1996, **77**, 3865.
23 G. Makov and M. C. Payne, *Phys. Rev. B: Condens. Matter Mater. Phys.*, 1995, **51**, 4014.
24 K. P. Huber and G. Herzberg, *Molecular Spectra and Molecular - Structure IV. Constants of Diatomic Molecules*, Van Nostrand Reinhold Company, 1978.
25 A. R. Akbarzadeh, I. Kornev, C. Malibert, L. Bellaiche and J. M. Kiat, *Phys. Rev. B: Condens. Matter Mater. Phys.*, 2005, **72**, 205104.
26 G. Henkelman, B. P. Uberuaga and H. Jónsson, *J. Chem. Phys.*, 2000, **113**, 9901.
27 S. C. Middleburgh, D. C. Parfitt, R. W. Grimes, B. Dorado, M. Bertolus, P. R. Blair, L. Hallstadius and K. Backman, *J. Nucl. Mater.*, 2012, **420**, 258–261.
28 J. Robertson, *J. Vac. Sci. Technol., B: Microelectron. Nanometer Struct.–Process., Meas., Phenom.*, 2000, **18**, 1785.
29 M. Cherry, M. S. Islam and C. R. A. Catlow, *J. Solid State Chem.*, 1995, **118**, 125–132.
30 M. S. Islam, *J. Mater. Chem.*, 2000, **10**, 1027–1038.
31 B. S. Thomas, N. A. Marks and B. D. Begg, *Nucl. Instrum. Methods Phys. Res., Sect. B*, 2007, **254**, 211–218.
32 S. J. Stokes and M. S. Islam, *J. Mater. Chem.*, 2010, **20**, 6258–6264.
33 O. Kamishima, T. Hattori, K. Ohta, Y. Chiba and M. Ishigame, *J. Phys.: Condens. Matter*, 1999, **11**, 5355–5365.
34 A. Slodczyk, M.-H. Limage, P. Colomban, O. Zaafrani, F. Grasset, J. Loricourt and B. Sala, *J. Raman Spectrosc.*, 2011, **42**, 2089–2099.
35 F. A. Rabuffetti and R. L. Brutchey, *ACS Nano*, 2013, **7**, 11435–11444.
36 G. Hautier, S. P. Ong, A. Jain, C. J. Moore and G. Ceder, *Phys. Rev. B: Condens. Matter Mater. Phys.*, 2012, **85**, 155208.
37 J. H. Linsford, X. Yang, K. Haller, J. Laane, G. Mestl and H. Knözinger, *J. Phys. Chem.*, 1993, **79**, 13810–13813.
38 A. Ianoul, T. Coleman and S. A. Asher, *Anal. Chem.*, 2002, **74**, 1458–1461.
39 H. Chen and N. Umezawa, *Phys. Rev. B: Condens. Matter Mater. Phys.*, 2014, **90**, 035202.

